ROYAL SOCIETY
OF CHEMISTRY

COMMUNICATION

Check for updates

Oxidizing solid Co into hollow Co₃O₄ within electrospun (carbon) nanofibers towards enhanced lithium storage performance†

Jinkai Wang,[a] Hongkang Wang, [ID] *[a] Fang Li,[a] Sanmu Xie,[a] Guiyin Xu, [ID] [d] Yiyi She,[c] Micheal K. H. Leung [ID] [c] and Tianxi Liu[b]

Transition metal oxides (TMOs) have been regarded as promising anode materials for lithium-ion batteries (LIBs) owing to their high theoretical capacities, natural abundance, and eco-friendliness. However, their large volume changes and the thus resulting pulverization problem, as well as the poor electrical conductivity, have hindered their practical applications. Design of hollow nanostructures with simultaneous carbon hybridization has shown great promise to overcome these drawbacks. Herein, we demonstrate a facile strategy to fabricate hollow Co₃O₄ nanoparticle-assembled nanofibers with controllable carbon content *via* electrospinning and subsequent annealing. Interestingly, the solid Co nanoparticles encapsulated within carbon nanofibers convert into hollow Co₃O₄ counterparts under ambient oxidation in air, and the carbon content can be easily adjusted by controlling the annealing temperature/time. When used as anode materials for LIBs, the hollow Co₃O₄ nanoparticle-assembled nanofibers (no carbon left) deliver a high discharge capacity of 1491.5 mA h g⁻¹ after 180 cycles at 200 mA g⁻¹, demonstrating superior lithium storage properties. Notably, optimized Co₃O₄/C nanofibers with 10 wt% carbon content demonstrate superior cycling stability, delivering a stable reversible capacity of ∼871.5 mA h g⁻¹ after 500 cycles at 200 mA g⁻¹. The superior electrochemical performance of the Co₃O₄(/C) nanofibers could be ascribed to the unique hollow nanostructure of Co₃O₄, the carbon hybridization, and the novel hierarchical nanoparticle-nanofiber assembly, which could not only shorten the lithium diffusion length, but also efficiently buffer the volumetric changes upon repeated lithiation/delithiation processes.

Lithium-ion batteries (LIBs), as some of the most promising rechargeable energy storage devices, have been widely used in portable electronics owing to their low cost, environmental friendliness, long cycle life, and high energy density.[1–3] With continuous technological advancement, LIBs with higher energy/power densities and longer lifespan are urgently needed, especially in the fields of electric vehicles and smart-grids.[4,5] Currently, graphite-based anode materials are commercially dominant owing to their excellent cycling performance, but they possess a low theoretical capacity of only 372 mA h g⁻¹, limiting their large-scale energy storage applications.[4,6]

Transition metal oxides (TMOs) have been attracting increasing interest due to their high theoretical specific capacities, natural abundance, and eco-friendliness. As a typical TMO, Co₃O₄ exhibits a high theoretical capacity of 890 mA h g⁻¹ according to the reversible conversion reaction of Co₃O₄ + 8Li⁺ + 8e⁻ ↔ 3Co + 4Li₂O.[7] However, it suffers from a large volume expansion/contraction and poor electrical conductivity, which lead to largely irreversible capacity loss and poor cycling stability.[8] In order to alleviate the volume change induced stress and the thus resulting pulverization problem, rational structure design of Co₃O₄ is critically important, and nanostructuring has been suggested as a promising strategy, as it can greatly shorten the lithium diffusion length, and efficiently facilitate the electrode/electrolyte interfacial reactions.[9–11] To date, various nanostructured Co₃O₄ materials have been prepared and investigated as LIB anodes, such as nanotubes,[8,12,13] nanowires,[14] nanosheets,[15] nanoparticles,[16] nanocages, and so on.[17–19] To enhance the electrical conductivity, hybridizing TMOs with carbon-based materials has been widely used. Even though great advancements have been made through various strategies, the long-term cycling stability of Co₃O₄-based anodes is still far from satisfactory and needs further improvement.

[a]State Key Lab of Electrical Insulation and Power Equipment, Center of Nanomaterials for Renewable Energy (CNRE), School of Electrical Engineering, Xi'an Jiaotong University, Xi'an 710049, People's Republic of China. E-mail: hongkang.wang@mail.xjtu.edu.cn

[b]State Key Laboratory for Modification of Chemical Fibers and Polymer Materials, College of Materials Science and Engineering, Donghua University, Shanghai 201620, People's Republic of China

[c]Ability R&D Energy Research Centre (AERC), School of Energy and Environment, City University of Hong Kong, Hong Kong SAR, People's Republic of China

[d]Department of Nuclear Science and Engineering, Department of Materials Science and Engineering, Massachusetts Institute of Technology, Cambridge, Massachusetts 02139, USA

Hollow nanomaterials have attracted considerable attention owing to their unique structural characteristics (*eg.*, large specific surface area, high porosity, *etc.*) and physicochemical properties (*eg.*, superior chemical and thermal stability, high reactivity, *etc.*), and they exhibit promising applications in catalysis,[20] sensing,[21] and energy storage.[22–25] Especially in LIBs, a hollow structure can effectively buffer the volumetric expansion/contraction during the lithiation/delithiation process, thus improving the electrochemical performance.[22,30,31] So far, most hollow nanostructures have been prepared *via* a template method or the Kirkendall-diffusion process in solution phases.[26] Recently, solid-to-hollow transformation has been observed under ambient atmosphere in *in situ* transmission electron microscopy (TEM) studies.[27–29] For example, Yu *et al.* observed the phase/shape evolutions from solid Ni nanoparticles to hollow NiO nanoparticles under ambient pressure.[29] Xia *et al.* also observed the oxidation of Ni–Fe bimetallic nanoparticles into hollow oxides *via in situ* TEM.[28] Herein, we demonstrate the ambient oxidation of solid Co nanoparticles into hollow Co_3O_4 nanoparticles in electrospun (carbon) nanofibers, through a facile strategy of electrospinning and subsequent annealing in air. The novel hierarchical assembly of hollow Co_3O_4 nanoparticles in a fibrous structure with controlled carbon content can be readily engineered by adjusting the oxidation temperature/time. When used as anode materials for LIBs, the fibrous products exhibited high specific capacity and superior cycling stability due to their unique hollow nanostructure, the carbon hybridization, and the novel hierarchical nanoparticle-nanofiber assembly.

Fig. 1a schematically illustrates the syntheses of the Co nanoparticles encapsulated in carbon nanofibers (denoted as Co@C) and the hollow Co_3O_4 nanoparticle assembled nanofibers (denoted as Co_3O_4 nanofibers in short) *via* electrospinning and subsequent annealing. In a typical synthesis, cobalt(II) acetate ($Co(Ac)_2$), dicyandiamide (DCD, $C_2H_4N_4$), and polyacrylonitrile (PAN) were used as the Co source, additive and carbon source, respectively, which were dissolved in *N,N*-dimethylformamide (DMF) serving as the electrospinning precursor solution. Thus the $Co(Ac)_2$/DCD/PAN precursor nanofibers (Fig. S1†) can be easily prepared *via* a facile electrospinning route. Then, the Co@C nanofibers were obtained by annealing the electrospun $Co(Ac)_2$/DCD/PAN nanofibers at 700 °C under an Ar atmosphere for 2 h. During this step, PAN was carbonized into carbon, serving as a reducing agent to reduce $Co(Ac)_2$ into metallic Co nanoparticles. In the third step of oxidation of Co@C nanofibers under ambient atmosphere, the solid Co nanoparticles were converted into hollow Co_3O_4 nanoparticles under a low annealing temperature in air. Note that nanosized Co particles with high activity easily burn, producing higher energy to ignite carbon nanofibers and thus resulting in the formation of porous Co_3O_4 nanofibers. In the XRD patterns of Co@C nanofibers, three diffraction peaks located at 44.2, 51.5, and 75.8° can be well indexed to the (111), (200), and (220) planes of the cubic Co (JCPDS no. 15-0806), respectively. However, the three typical peaks belonging to Co metal completely disappear after annealing in air. Instead, all diffraction peaks in the Co_3O_4 nanofibers can be attributed to the cubic Co_3O_4 phase (JCPDS no. 43-1003).
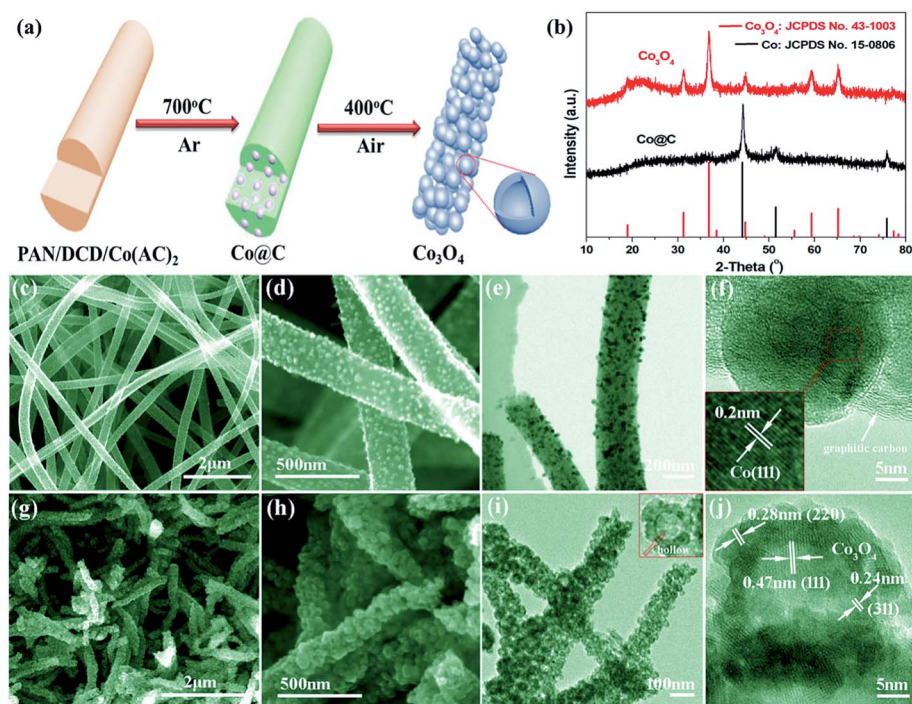

Fig. 1 (a) Schematic illustration of the synthesis of fibrous Co_3O_4 with a hollow and porous structure from the electrospun $Co(Ac)_2$/DCD/PAN and Co@C nanofibers by annealing under different conditions. (b) XRD patterns of the as-prepared Co@C and Co_3O_4 nanofibers. (c and d) SEM, (e) TEM and (f) HRTEM images of the as-prepared Co@C nanofibers. (g and h) SEM, (i) TEM and (j) HRTEM images of the as-prepared Co_3O_4 nanofibers.

The morphological and microstructural characteristics of the Co@C and Co_3O_4 nanofibers were examined *via* scanning electron microscopy (SEM) and transmission electron microscopy (TEM) analyses. Fig. 1c and d show the SEM images of the Co@C nanofibers, which exhibit lengths of tens of micrometers and an average diameter of around 200 nm. Combined with the TEM image (Fig. 1e), it can be apparently observed that numerous Co nanoparticles are either homogeneously embedded into the carbon nanofibers or anchored on the surface regions. As shown in the HRTEM image (Fig. 1f), the carbon nanofibers show obvious graphitic crystallization, and the lattice fringes with a *d* spacing of 0.34 nm correspond to the (002) plane of hexagonal graphite.[30,31] Besides, the embedded Co nanoparticles with a size of tens of nanometers show a lattice spacing of 0.2 nm, which can be indexed to the (111) reflections of the cubic Co phase (inset of Fig. 1f). After annealing in air (Fig. 1g–i), the as-prepared Co_3O_4 still shows a well-preserved fibrous morphology with lengths of several to tens of micrometers and an average diameter of around 200 nm. Interestingly, the Co_3O_4 nanofibers are assembled by numerous smaller nanoparticles with a clear hollow interior (Fig. 1i and j). As shown in the HRTEM image (Fig. 1j), the lattice fringes with *d* spacings of 0.47, 0.28, and 0.24 nm can be well indexed to the (111), (220), and (311) planes of the Co_3O_4 phase, respectively, indicating the polycrystalline nature of the hollow Co_3O_4 nanoparticles.

Raman spectroscopy and thermogravimetric analysis (TGA) were performed to trace the carbon evolution. Fig. 2a compares the Raman spectra of Co@C and Co_3O_4 nanofibers. In the Raman spectrum of Co@C nanofibers, two apparent peaks at approximately 1337 and 1596 cm^{-1} are observed, corresponding

to the amorphous/defective carbon species (D peak) and the ordered graphitic carbon species (G peak), respectively. The I_D/I_G intensity ratio for the Co@C nanofibers was around 1.48, indicating the disordered carbon structure.[32] Notably, both peaks corresponding to the carbon disappear in the Co_3O_4 nanofibers, indicating the complete combustion of carbon matrices after annealing in air. Instead, the newly emerged peaks located at 191.3, 466.1, 511.8 and 674.2 cm^{-1} can be well assigned to the F_{2g}^1, E_g, F_{2g}^2 and A_{1g} modes of Co_3O_4, respectively, which relate to the expansion and contraction vibration modes of Co–O bonds.[33] In addition, the TGA analysis further confirms that the carbon was lost after annealing Co@C nanofibers in air. Interestingly, the TGA curve of Co@C nanofibers shows an abrupt weight loss at around 275 °C, indicating that the oxidation of Co into Co_3O_4 is pretty fast. According to the chemical reaction (inset in Fig. 2b), the carbon content in the Co@C nanofibers can be calculated to be as high as ~64.0 wt%. The specific surface area and the pore structures of the Co@C and Co_3O_4 nanofibers were investigated using N_2 adsorption–desorption isotherms (Fig. 2c and d). The Co@C nanofibers possess a high specific surface area of 420.5 $m^2\ g^{-1}$ with an average pore size of 5.6 nm and a pore volume of 0.55 $cm^3\ g^{-1}$, which is beneficial for the oxidation reaction. In contrast, the Co_3O_4 nanofibers show a decreased specific surface area of 63.5 $m^2\ g^{-1}$ but an increased average pore size of 20.4 nm and a pore volume of 0.35 $cm^3\ g^{-1}$. Note that the average pore size is consistent with the pore size of the hollow Co_3O_4 nanoparticles, which further confirms the solid–hollow conversion.

The chemical compositions and the chemical states of the Co@C and Co_3O_4 nanofibers were examined by XPS analysis (Fig. S2†). As shown in Fig. 2e, the core-level Co $2p_{1/2}$ and $2p_{3/2}$
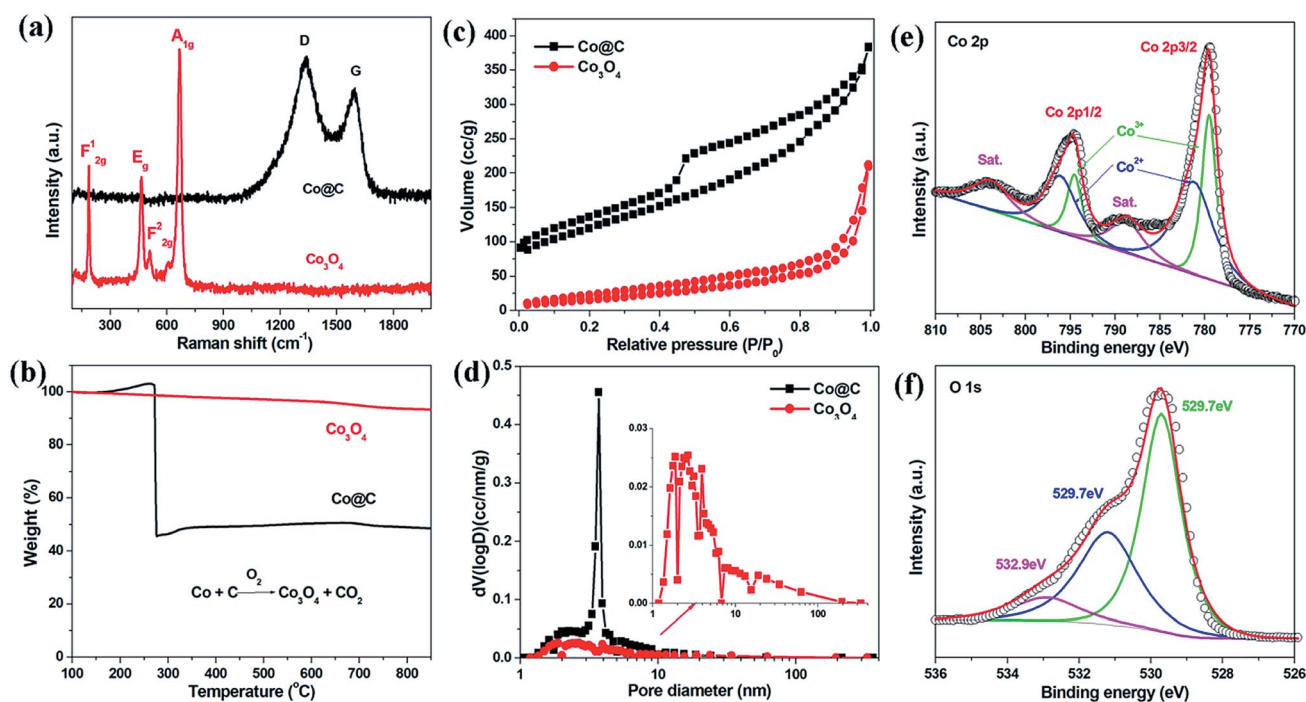

Fig. 2 (a) Raman spectra, (b) TGA curves, (c) N_2 sorption isotherms, and (d) pore size distribution plots for the Co@C and Co_3O_4 nanofibers. (e and f) High-resolution XPS spectra of (e) Co 2p and (f) O 1s for the Co_3O_4 nanofibers.

peaks are clearly observed in the Co 2p spectrum at around 794.7 and 779.5 eV, respectively. Besides, two satellite peaks for the $2p_{1/2}$ and $2p_{3/2}$ levels locate at approximately 804.0 and 788.7 eV, respectively. These peaks are the typical characteristics for Co_3O_4 nanostructures.[34] As revealed by the deconvoluted peaks of Co 2p, both Co^{2+} and Co^{3+} are present in the Co_3O_4 nanofibers (Fig. 2e), and the cobalt content with the Co^{3+} valence state can be roughly estimated as ~37%. Fig. 2f shows the deconvoluted O 1s XPS spectrum, where three oxygen contributions can be revealed. The peak at ~529.7 eV is typical for metal–oxygen bonds, while the peak at ~531.2 eV arises from oxygen vacancy defects as well as surface adsorbed oxygen species (eg., uncoordinated lattice oxygen and hydroxyls). The peak at ~532.9 eV may be ascribed to the physi-/chemisorbed water at the surface region.[33]

In order to explore the structural evolution of the solid to hollow transition in the nanofibers, time/temperature-dependent experiments were also performed by appropriately annealing the Co@C nanofibers under ambient atmosphere (Fig. 3). Interestingly, even when annealing the Co@C nanofibers at 300 °C for 15 min (Fig. 3a and b), hollow nanospheres were produced and embedded within the carbon nanofibers, in which the carbon content is ~32 wt% (Fig. S3†). With increasing the reaction time, the carbon content decreases gradually as revealed by the TGA analysis (Fig. S3a†), which greatly affects the lithium storage performance of the resultant products (Fig. S3b†). After annealing in air at 300 °C for 3 h, the carbon content was decreased to ~10 wt%, and the hollow Co_3O_4 nanoparticles can be clearly observed at the interfacial region (Fig. 3c and d), which may be related to the sufficient oxygen contact and the thus resulting fast reaction rate.

The electrochemical properties of the Co@C and Co_3O_4 nanofibers as anode materials for LIBs were investigated using lithium foil as the counter electrode. Fig. 4a shows the first five cyclic voltammetry (CV) curves of the Co_3O_4 nanofibers at a scan rate of 0.2 mV s^{-1} (Fig. S4†). In the initial cathodic scan, a weak reduction peak located at ~1.1 V can be observed, which is attributed to the formation of intermediate $Li_xCo_3O_4$ (Co_3O_4 + xLi$^+$ → $Li_xCo_3O_4$).[35] Besides, there is also a sharp cathodic peak observed at ~0.8 V, which is associated with the conversion of ionic Co to metallic Co ($Li_xCo_3O_4$ + $(8 - x)$Li$^+$ → 3Co + $4Li_2O$) and the formation of a solid electrolyte interphase (SEI) film.[36] In the first anodic scan, the peak at around 2.1 V is attributed to the oxidation of metallic Co into Co_3O_4, which agrees well with other Co_3O_4 materials (3Co + $4Li_2O$ → Co_3O_4 + 8Li$^+$ + $8e^-$).[7] In addition, from the second CV cycle onward, the cathodic peaks slightly shift and split into two broad peaks at about 0.95 and 1.15 V, respectively. This may be related to the activation process and the structure reorganization of the electrode materials after Li$^+$ insertion/extraction in the first cycle.[37] Moreover, the CV curves overlap very well in the subsequent CV cycles, suggesting the good cycling stability and superior reversibility during the Li$^+$ insertion/extraction processes.

The charge storage mechanism was further studied by CV analysis, and Fig. 4b shows the CV curves of the Co_3O_4 electrode at different scan rates ranging from 0.1 to 1.0 mV s^{-1}. It is observed that there are two cathodic peaks between 0.95 and 1.31 V at a lower scan rate of 0.1 mV s^{-1}, which gradually merge into one broad peak with increasing the scan rate from 0.1 to 1.0 mV s^{-1}, suggesting the kinetics limitation arising from the limited relaxation time for a stepwise phase evolution during the rapid scanning.[38] According to the formula $i = av^b$ (i is the peak current and v is the scan rate in a CV curve), the lithium storage mechanism can be revealed by analyzing the relationship between the peak current and the scan rate. The value of b relies on the solvated ion storage mechanism ($b = 0.5$ means a diffusion-controlled process, while $b = 1$ means a pseudocapacitive process).[39] Fig. 4c shows the corresponding log–log relationship between the peak current and scan rate with a linear relation, and the b values for the prominent anodic peak and cathodic peak are calculated as 0.64 and 0.68, respectively, indicating that the electrochemical reaction in the Co_3O_4 electrode is diffusion-controlled but also with pseudocapacitive behaviors.

Fig. 4d shows the galvanostatic charge–discharge profiles of the Co_3O_4 electrode in the voltage range of 0.01–3.0 V at 200 mA g^{-1}. The initial specific discharge/charge capacities are 1383.3/922.3 mA h g^{-1}, with an initial coulombic efficiency (ICE) of 66.7%, and the irreversible capacity loss of the Co_3O_4 electrode may mainly result from the formation of the SEI film. Notably, both the discharge/charge capacities successively increase with increasing cycle number, which indicates the gradual activation of the electrode materials. This phenomenon is quite common in the transition metal compound-based anodes as revealed in the previous literature.[30,40–43] Such a capacity increase upon cycling can be ascribed to the successive electrode activation and the thus resulting exposure of more active sites after repeated lithium insertion/extraction. Moreover, the in situ generated transition metal nanograins during the conversion reaction can catalyze the decomposition of the electrolyte and result in the formation of a polymer/gel-like film, which can provide additional lithium storage capacity with the actual capacity far beyond the theoretical value.[44,45]

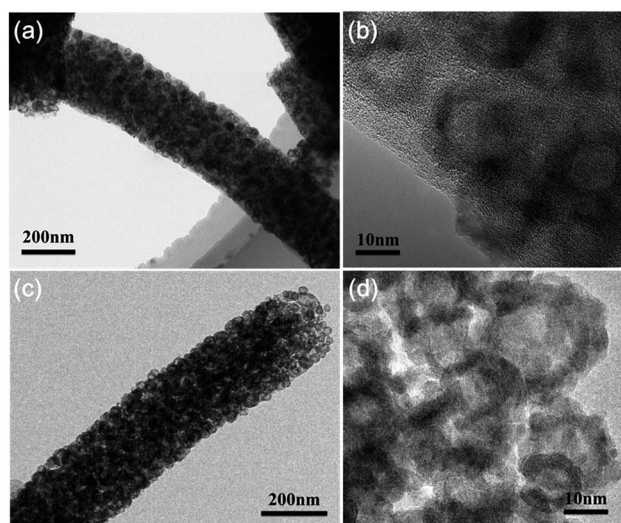

Fig. 3 TEM images for the intermediate products obtained by annealing Co@C nanofibers at 300 °C in air for different time durations. (a and b) 15 min; (c and d) 3 h.
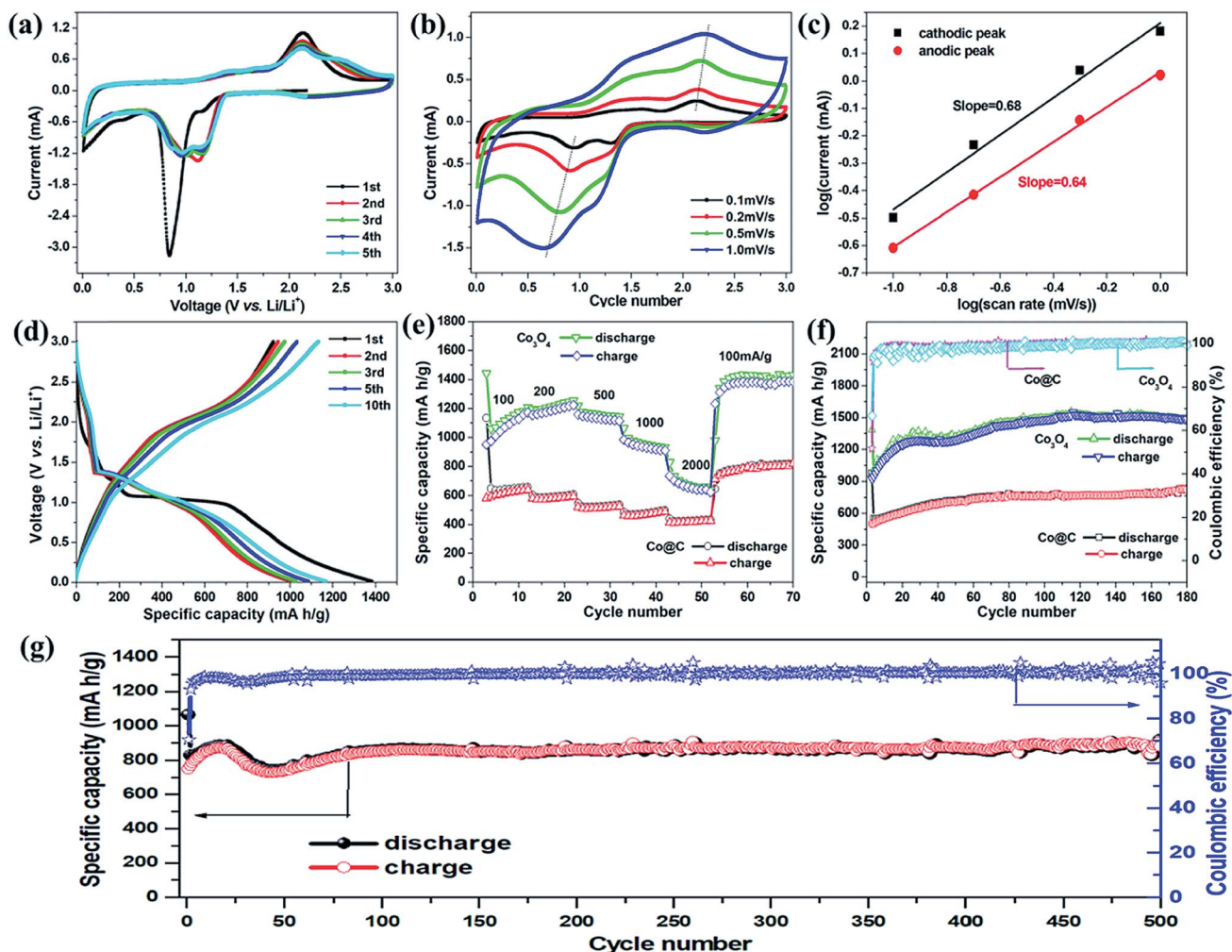
Fig. 4 Electrochemical properties of the Co@C and Co_3O_4 nanofibers. (a) CV curves at 0.2 mV s^{-1}, (b) CV curves of the Co_3O_4 electrode at different scan rates and (c) the corresponding log−log relationship between the peak current and scan rate. (d) Discharge−charge profiles at 200 mA g^{-1} for the Co_3O_4 nanofibers; (e) rate performance at different current densities and (f) cycling performance at 200 mA g^{-1} for Co@C and Co_3O_4 nanofibers. (g) Long-term cycling performance with corresponding coulombic efficiencies of optimized Co_3O_4/C nanofibers obtained by annealing Co@C nanofibers at 300 °C in air for 3 h.

Fig. 4e compares the rate performance of Co@C and Co_3O_4 nanofibers at different current densities. The discharge capacities for the Co_3O_4 electrode are 1206.8, 1254.1, 1147.8, 933.6 and 658.6 mA h g^{-1} each after 10 cycles at current densities of 100, 200, 500, 1000 and 2000 mA g^{-1}, respectively, which are correspondingly higher than those of the Co@C electrode. When recovering the current density to 100 mA g^{-1}, the Co_3O_4 electrode even delivers a discharge capacity as high as ~1424.0 mA h g^{-1} after additional 20 cycles. Electrochemical impedance spectroscopy (EIS) analysis reveals that both Co@C and Co_3O_4 electrodes exhibit a small charge transfer resistance and high lithium diffusion rate (Fig. S5†), which is beneficial for the high rate capability. Moreover, Fig. 4f displays the cycling performance of the Co@C and Co_3O_4 electrodes at a current density of 200 mA g^{-1}. The Co@C and Co_3O_4 electrodes exhibit reversible specific capacities of ~820.5 and ~1491.5 mA h g^{-1} after 180 cycles, respectively. Note that the theoretical capacity of Co_3O_4 is widely regarded as 890 mA h g^{-1},[14,36,46,47] the

extremely high reversible lithium storage capacity of Co_3O_4 nanofibers could be attributed to the *in situ* formation of a polymer/gel-like film on the transition metal oxide anode, which provides a high pseudocapacitive capacity contribution in the low voltage region.[48,49]

As shown in Fig. 4f, the discharge/charge capacities of the Co_3O_4 nanofiber electrode start to decrease in the long-term cycling after 180 cycles, which may relate to the electrode pulverization owing to the absence of buffering carbon matrices, as they were completely combusted when annealing the Co@C nanofibers at 400 °C. As discussed above, the carbon matrices can be maintained by lowering the annealing temperature and shortening the annealing time in air. As a consequence, an optimized Co_3O_4/C nanofiber electrode was obtained by engineering the relative contents of Co_3O_4 and C, which displayed superior cycling stability (Fig. 4g), delivering a high reversible capacity of ~871.5 mA h g^{-1} after 500 cycles at 200 mA g^{-1}. Notably, the reported Co_3O_4(/C) nanofiber

electrodes showed better cycling performance than most of the previously reported electrodes (Table S1†).[12,36,50–53]

Especially, it's worth mentioning that the addition of DCD to the electrospinning precursor solution plays a vital role in the microstructures of the Co@C nanofibers (Fig. S6†) as well as the lithium storage performance of the resulting Co_3O_4 nanofibers. For comparison, the counterpart Co_3O_4 nanofibers were also obtained under the same reaction conditions but without the introduction of DCD (Fig. S7†), and they still exhibited the morphology of hollow Co_3O_4 nanoparticle assembled nanofibers but with low porosity. When used as an anode for LIBs, the as-prepared Co_3O_4 nanofibers with no DCD introduced also showed superior cycling/rate performance but with a relatively lower reversible capacity, delivering a discharge capacity of ~891.0 mA h g^{-1} after 200 cycles at 200 mA g^{-1} (Fig. S8†). More importantly, the current synthetic strategy can be generally applied to the fabrication of Ni and Ni–Co based hollow oxide nanoparticle assembled nanofibers (Fig. S9 and 10†), and all of them showed superior lithium storage performance (Fig. S11†).

Conclusions

In summary, we demonstrated the facile synthesis of a novel hierarchical hybrid nanostructure of hollow Co_3O_4 nanoparticle-assembled nanofibers with controllable carbon content *via* electrospinning and subsequent annealing. The time/temperature-dependent structure evolution experiments clearly revealed the ambient oxidation of Co nanoparticles into hollow Co_3O_4 counterparts, which were hierarchically assembled in the electrospun (carbon) nanofibers, and the carbon content can be readily controlled by adjusting the oxidation temperature/time. When examined as anodes for LIBs, the hollow Co_3O_4 nanoparticle-assembled nanofibers with no presence of carbon delivered the highest reversible capacity of 1491.5 mA h g^{-1} after 180 cycles at a current density of 200 mA g^{-1}, but they showed inferior long-term cycling stability. Notably, the optimized Co_3O_4/C nanofibers with ~10 wt% carbon content exhibited a reversible capacity of ~871.5 mA h g^{-1} after 500 cycles at 200 mA g^{-1}, demonstrating the excellent long-term cycling stability. Such a superior lithium storage performance of the Co_3O_4(/C) nanofibers can be attributed to their unique multidimensional hierarchical hybrid structure. The hollow Co_3O_4 nanoparticle assembled nanofibers with a porous structure and carbon hybridization can greatly shorten the lithium diffusion length, facilitate electrolyte/charge transport, and efficiently buffer the volumetric expansion and contraction upon repeated lithiation and delithiation processes. More importantly, the current strategy can also be applied to the synthesis of other transition metal (*eg.*, Ni, Ni–Co, *etc.*) oxides, which is promising for the design of novel high-performance nanostructured electrode materials for electrochemical energy storage and conversion applications.

Conflicts of interest

There are no conflicts to declare.

Acknowledgements

References

1 J. M. Tarascon and M. Armand, *Nature*, 2001, **414**, 359–367.
2 V. Etacheri, R. Marom, R. Elazari, G. Salitra and D. Aurbach, *Energy Environ. Sci.*, 2011, **4**, 3243–3262.
3 H. Wang, J. Wang, D. Cao, H. Gu, B. Li, X. Lu, X. Han, A. L. Rogach and C. Niu, *J. Mater. Chem. A*, 2017, **5**, 6817–6824.
4 H. Wang, X. Yang, Q. Wu, Q. Zhang, H. Chen, H. Jing, J. Wang, S.-B. Mi, A. L. Rogach and C. Niu, *ACS Nano*, 2018, **12**, 3406–3416.
5 Q. He, Y. Wang, X. X. Liu, D. J. Blackwood and J. S. Chen, *J. Mater. Chem. A*, 2018, **6**, 22115–22122.
6 E. Yoo, J. Kim, E. Hosono, H.-s. Zhou, T. Kudo and I. Honma, *Nano Lett.*, 2008, **8**, 2277–2282.
7 Z.-S. Wu, W. Ren, L. Wen, L. Gao, J. Zhao, Z. Chen, G. Zhou, F. Li and H.-M. Cheng, *ACS Nano*, 2010, **4**, 3187–3194.
8 X. W. Lou, D. Deng, J. Y. Lee, J. Feng and L. A. Archer, *Adv. Mater.*, 2008, **20**, 258–262.
9 C. Kim, K. S. Yang, M. Kojima, K. Yoshida, Y. J. Kim, Y. A. Kim and M. Endo, *Adv. Funct. Mater.*, 2006, **16**, 2393–2397.
10 Y. Chen, X. Li, K. Park, J. Song, J. Hong, L. Zhou, Y. W. Mai, H. Huang and J. B. Goodenough, *J. Am. Chem. Soc.*, 2013, **135**, 16280–16283.
11 L. Qie, W. M. Chen, Z. H. Wang, Q. G. Shao, X. Li, L. X. Yuan, X. L. Hu, W. X. Zhang and Y. H. Huang, *Adv. Mater.*, 2012, **24**, 2047–2050.
12 L. Zhuo, Y. Wu, J. Ming, L. Wang, Y. Yu, X. Zhang and F. Zhao, *J. Mater. Chem. A*, 2013, **1**, 1141–1147.
13 X. He, Y. Wu, F. Zhao, J. Wang, K. Jiang and S. Fan, *J. Mater. Chem. A*, 2013, **1**, 11121–11125.
14 Y. Li, B. Tan and Y. Wu, *Nano Lett.*, 2008, **8**, 265–270.
15 S. Q. Chen and Y. Wang, *J. Mater. Chem.*, 2010, **20**, 9735–9739.
16 Y. Kim, J.-H. Lee, S. Cho, Y. Kwon, I. In, J. Lee, N.-H. You, E. Reichmanis, H. Ko, K.-T. Lee, H.-K. Kwon, D.-H. Ko, H. Yang and B. Park, *ACS Nano*, 2014, **8**, 6701–6712.
17 J. Liu, H. Xia, L. Lu and D. Xue, *J. Mater. Chem.*, 2010, **20**, 1506.
18 N. Yan, L. Hu, Y. Li, Y. Wang, H. Zhong, X. Hu, X. Kong and Q. Chen, *J. Phys. Chem. C*, 2012, **116**, 7227–7235.

19 Y. Han, M. Zhao, L. Dong, J. Feng, Y. Wang, D. Li and X. Li, *J. Mater. Chem. A*, 2015, **3**, 22542–22546.

20 X. Fang, X. Zhao, W. Fang, C. Chen and N. Zheng, *Nanoscale*, 2013, **5**, 2205–2218.

21 J.-H. Lee, *Sens. Actuators, B*, 2009, **140**, 319–336.

22 Z. Wang, L. Zhou and X. W. David Lou, *Adv. Mater.*, 2012, **24**, 1903–1911.

23 W.-M. Zhang, J.-S. Hu, Y.-G. Guo, S.-F. Zheng, L.-S. Zhong, W.-G. Song and L.-J. Wan, *Adv. Mater.*, 2008, **20**, 1160–1165.

24 X. W. Lou, L. A. Archer and Z. Yang, *Adv. Mater.*, 2008, **20**, 3987–4019.

25 J. Hu, M. Chen, X. Fang and L. Wu, *Chem. Soc. Rev.*, 2011, **40**, 5472–5491.

26 Y. Yin, R. M. Rioux, C. K. Erdonmez, S. Hughes, G. A. Somorjai and A. P. Alivisatos, *Science*, 2004, **304**, 711–714.

27 Q. Yu, M. M. Mao, Q. J. Li, X. Q. Fu, H. Tian, J. X. Li, S. X. Mao and Z. Zhang, *Nano Lett.*, 2016, **16**, 1156–1160.

28 W. Xia, Y. Yang, Q. Meng, Z. Deng, M. Gong, J. Wang, D. Wang, Y. Zhu, L. Sun, F. Xu, J. Li and H. L. Xin, *ACS Nano*, 2018, **12**, 7866–7874.

29 J. Yu, W. Yuan, H. Yang, Q. Xu, Y. Wang and Z. Zhang, *Angew. Chem., Int. Ed.*, 2018, **57**, 11344–11348.

30 H. Wang, J. Wang, S. Xie, W. Liu and C. Niu, *Nanoscale*, 2018, **10**, 6159–6167.

31 J. Wang, H. Wang, D. Cao, X. Lu, X. Han and C. Niu, *Part. Part. Syst. Charact.*, 2017, **34**, 1700185.

32 Y. Li, X. Lu, H. Wang, C. Xie, G. Yang and C. Niu, *Electrochim. Acta*, 2015, **178**, 778–785.

33 M. David, G. Hugh, C. Elaine, G. Shane, L. Alex and O. D. Colm, *Mater. Res. Express*, 2017, **4**, 025011.

34 W. Kang, Y. Zhang, L. Fan, L. Zhang, F. Dai, R. Wang and D. Sun, *ACS Appl. Mater. Interfaces*, 2017, **9**, 10602–10609.

35 M. Jing, M. Zhou, G. Li, Z. Chen, W. Xu, X. Chen and Z. Hou, *ACS Appl. Mater. Interfaces*, 2017, **9**, 9662–9668.

36 S. Abouali, M. Akbari Garakani, B. Zhang, H. Luo, Z.-L. Xu, J.-Q. Huang, J. Huang and J.-K. Kim, *J. Mater. Chem. A*, 2014, **2**, 16939–16944.

37 G. Gao, H. B. Wu and X. W. D. Lou, *Adv. Energy Mater.*, 2014, **4**, 1400422.

38 X. Yang, J. Wang, S. Wang, H. Wang, O. Tomanec, C. Zhi, R. Zboril, D. Y. W. Yu and A. Rogach, *ACS Nano*, 2018, **12**, 7397–7405.

39 X. Xia, D. Chao, Y. Zhang, J. Zhan, Y. Zhong, X. Wang, Y. Wang, Z. X. Shen, J. Tu and H. J. Fan, *Small*, 2016, **12**, 3048–3058.

40 J. Wang, H. Wang, D. Cao, X. Lu, X. Han and C. Niu, *Part. Part. Syst. Charact.*, 2017, **34**, 1700185.

41 K. Chang, D. Geng, X. Li, J. Yang, Y. Tang, M. Cai, R. Li and X. Sun, *Adv. Energy Mater.*, 2013, **3**, 839–844.

42 Z. Li, H. Xue, J. Wang, Y. Tang, C.-S. Lee and S. Yang, *ChemElectroChem*, 2015, **2**, 1682–1686.

43 W. Wei, S. Yang, H. Zhou, I. Lieberwirth, X. Feng and K. Mullen, *Adv. Mater.*, 2013, **25**, 2909–2914.

44 D. Cao, H. Wang, B. Li, C. Li, S. Xie, A. L. Rogach and C. Niu, *Electrochim. Acta*, 2016, **216**, 79–87.

45 L. Fan, W. Zhang, S. Zhu and Y. Lu, *Ind. Eng. Chem. Res.*, 2017, **56**, 2046–2053.

46 B. Wang, X.-Y. Lu, C.-W. Tsang, Y. Wang, W. K. Au, H. Guo and Y. Tang, *Chem. Eng. J.*, 2018, **338**, 278–286.

47 D. Gu, W. Li, F. Wang, H. Bongard, B. Spliethoff, W. Schmidt, C. Weidenthaler, Y. Xia, D. Zhao and F. Schuth, *Angew. Chem., Int. Ed.*, 2015, **54**, 7060–7064.

48 B. Wang, J. S. Chen, H. B. Wu, Z. Wang and X. W. Lou, *J. Am. Chem. Soc.*, 2011, **133**, 17146–17148.

49 S. Laruelle, S. Grugeon, P. Poizot, M. Dolle, L. Dupont and J. M. Tarascon, *J. Electrochem. Soc.*, 2002, **149**, A627–A634.

50 J. Wang, N. Yang, H. Tang, Z. Dong, Q. Jin, M. Yang, D. Kisailus, H. Zhao, Z. Tang and D. Wang, *Angew. Chem., Int. Ed.*, 2013, **52**, 6417–6420.

51 L. Wang, Y. Zheng, X. Wang, S. Chen, F. Xu, L. Zuo, J. Wu, L. Sun, Z. Li, H. Hou and Y. Song, *ACS Appl. Mater. Interfaces*, 2014, **6**, 7117–7125.

52 J. Sun, H. Liu, X. Chen, D. G. Evans and W. Yang, *Nanoscale*, 2013, **5**, 7564–7571.

53 L. Lai, J. Zhu, Z. Li, D. Y. W. Yu, S. Jiang, X. Cai, Q. Yan, Y. M. Lam, Z. Shen and J. Lin, *Nano Energy*, 2014, **3**, 134–143.